4

Properties of Hard Carbon Coatings Manufactured on Magnesium Alloys by PACVD Method

Marcin Golabczak
Technical University of Lodz, Department of Production Engineering
Poland

1. Introduction

Magnesium alloys found a plethora of applications in various branches of industry where reduction in weight is of importance (Gray & Luan, 2002). These alloys are used in aerospace, automobile and electronic industries, for manufacturing of sporting goods etc. Advantages of magnesium alloys include: the high strength: weight ratio, high thermal conductivity, small heat extensibility, good welding characteristics and high functional integrity, which allow to produce near-net-shape elements as well as good machinability (Hawkins, 1993). However, magnesium alloys have also certain disadvantages. The most troublesome of them is the high susceptibility to corrosion, which contributes to dwindling of their size and reduces mechanical durability. Other disadvantages of magnesium alloys comprise their weak wear resistance, a drop in durability at high temperature and interference of electromagnetic field. The aforementioned faults considerably reduce the area of application of this material.
Presented studies aimed at elimination of the listed drawbacks by means of covering of magnesium alloy AZ31 with special hard carbon coatings to form a protective barrier with decorative appearance. Plasma Activated Chemical Vapor Deposition (PACVD) method was used for this purpose. Optimum conditions of this process were determined and the material properties of the coatings were characterized.

2. Experimental apparatus and procedure

Hard carbon films were deposited on magnesium alloys AZ31 by PACVD method, which relied on decomposition of methane in electric field with high frequency of 13.56 MHz, obtained at the pressure of approximately 12 Pa in a working chamber (Golabczak, 2005). Processes of PACVD were realized in the stand presented in figure 1. It consisted of the chamber of water cooled plasma reactor, the high frequency electrode fixed to the plate of the base and connected through the condenser (the latter provided the negative potential of self-polarization), generator of high frequency (facilitated production of plasma with high density and maintained the frequency at the constant level), vacuum system and systems of measurement and control.
Hard carbon coatings were deposited on magnesium alloy AZ31 in two steps comprising the process of ionic digestion of their surface followed by the process of synthesis of these coatings. Parameters of these steps are shown in table 1.

Fig. 1. The scheme of the system used for deposition of hard carbon coatings by PACVD method

Parameter	Ionic digestion of the surface	Process of coating deposition
Feed gas	CH_4	CH_4
Pressure in a working chamber	8 ÷ 10 Pa	12 Pa
Time of process - t	4 min	5 ÷ 9 min
Gas flow rate - V	5 cm^3/ min	20÷60 cm^3/ min

Table 1. Parameters of PACVD process

3. Results and discussion

The experiments included optimization of technological parameters of PACVD process of deposition of carbon films and characterization of their material properties. To determine the optimum condition of PACVD process a series of test specimens was produced according to the fractional experimental 2^{n-1} design (Golabczak, 2005). The studies of material properties of carbon coatings deposited on magnesium alloy AZ31 comprised determination of morphology of these coatings, measurements of their nanohardness and thickness (Golabczak & Konstantynowicz, 2010), tribologic tests and determination of their corrosion resistance.

3.1 Determination of morphology of hard carbon coatings deposited on a surface of magnesium alloy

Morphology of hard carbon coatings deposited on the surface of magnesium alloy AZ31 was determined on the basis of their Raman spectra (Golabczak, 2005). For this purpose, the mathematical modeling of fitting of gaussian peaks of the identified carbon phases to the Raman spectra was performed (Golabczak, 2005). The contents of the identified carbon

phases in the deposited carbon coatings were determined on the basis of the relative index - E_i, described by the following equation (1):

$$E_i = \frac{A_{p_i}}{A_s} = \frac{\int p_i(x)dx}{\sum\int p_i(x)dx} \tag{1}$$

where: A_{pi} - surface area between the baseline and the curve of fitting to the plot for the carbon phases identified in the coating, calculated by the method of numerical integration; A_s - the summary surface area between the baseline and the curve of fitting to Raman spectrum, calculated by the method of numerical integration (Golabczak, 2005).
Results of computing of the relative index E_i, obtained for each specimen prepared within the scope of the planned experiment, are shown in figure 2.

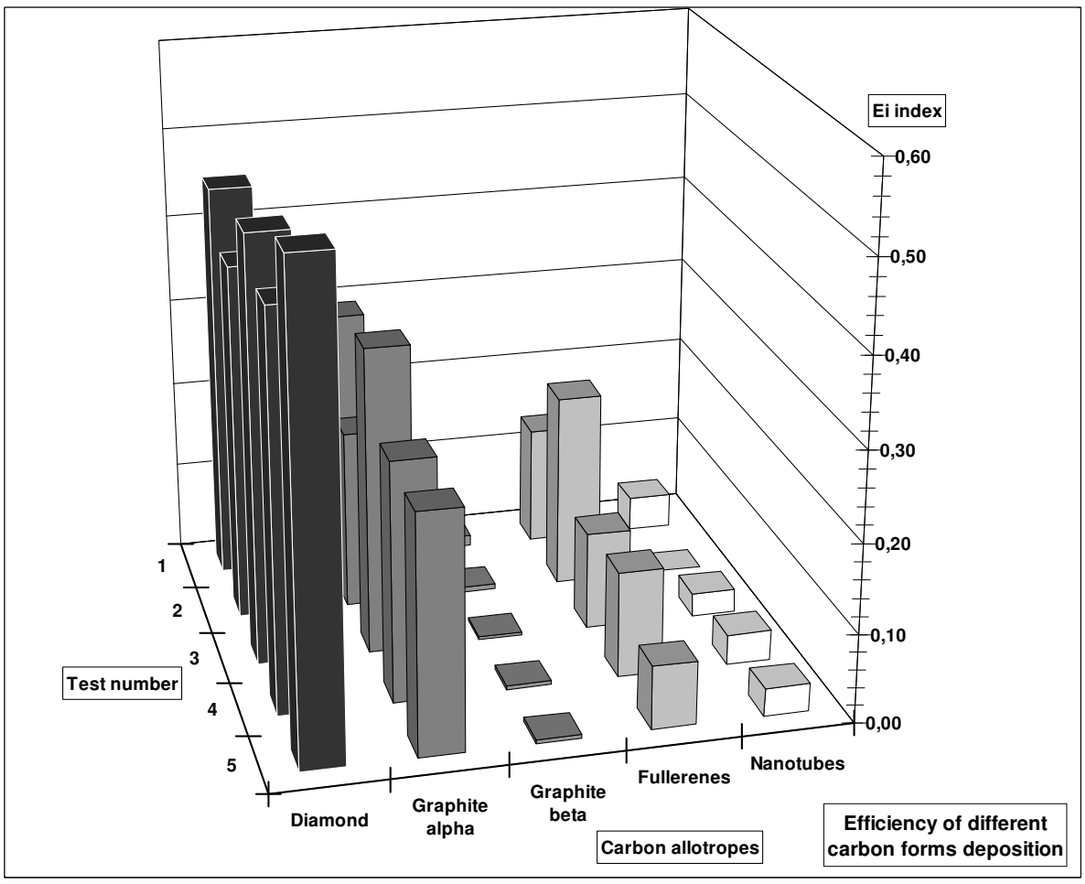

Fig. 2. Comparison of values of the relative index E_i for carbon phases identified in hard carbon coatings deposited on magnesium alloy specimens obtained within the scope of the planned experiments of PACVD process

Analysis of results obtained for individual specimens produced within the scope of the planned experiment (specimens 1÷4), revealed that the diamond phase (E_i=0.40÷0.48) and alfa-graphite phase (E_i=0.20÷0.35) dominated in the deposited coatings. Also other carbon phases were identified, such as beta-graphite- (E_i=0.003÷0.013), fullerens (E_i=0.11÷0.22),

nanotubes (E_i of approximately 0.034) and other, including some unidentified forms (E_i=0.006÷0.068), rings (E_i of approximately 0.008), and chains (E_i=0.018÷0.12), but their contents were minor. Optimization of deposition conditions (specimen 5) showed that the rise in contents of diamond phase (to E_i=0.54) in the coatings was achievable. The latter content of diamond phase in the coating was reached under the following PACVD process conditions: U=900V, t=8min, and V=60cm^3/ min.

3.2 Measurements of nanohardness of hard carbon coatings deposited on magnesium alloy AZ31

Nanohardness of hard carbon coatings was measured using Nano Test 600 meter (Micro Materials Ltd., Great Britain) equipped with a diamond pyramidal penetrator (Golabczak, 2005). The measurements of nanohardness were conducted at the penetrating force (F) of 0.1–0.6 mN (extorted by the penetrator) and the rate of F increase (dF/ dt) of 0.02 mN/ s. Values of nanohardness of hard carbon coatings, measured by using the pyramidal penetrator, were calculated as follows (2):

$$H_n = \frac{F}{24{,}5h_p^{\,2}} \tag{2}$$

where: H_n – nanohardness of the outer layer [GPa], F – the penetrating force [N], h_p – indentation made by the penetrator [m].

Representative results of nanohardness measurements of the examined hard carbon coatings deposited on magnesium alloy AZ31 are shown in figure 3.

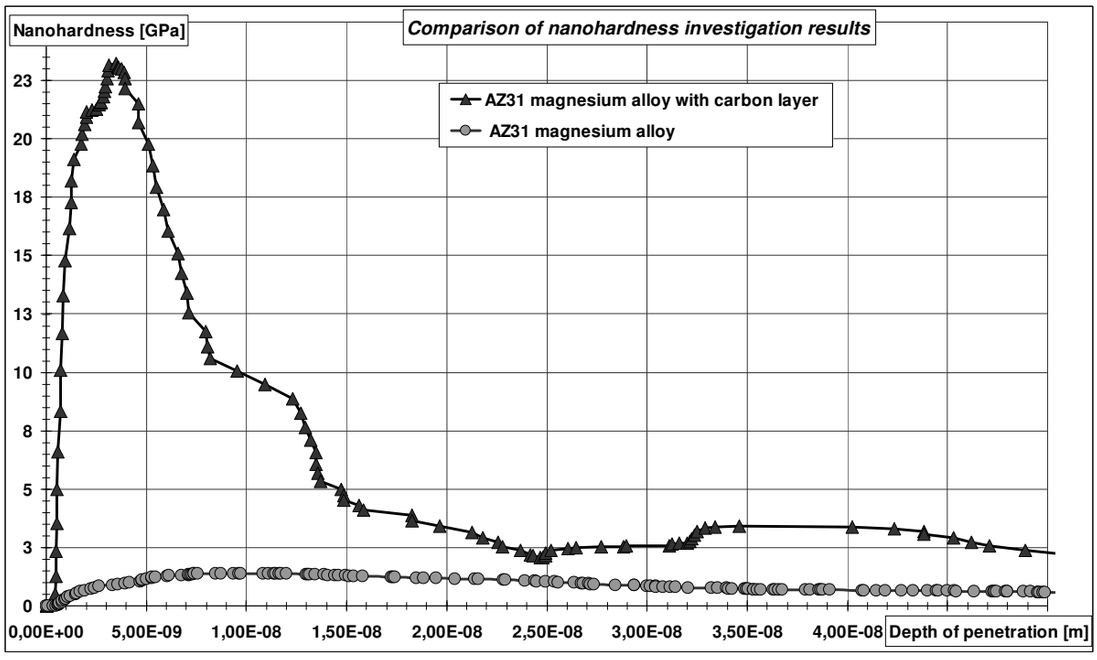

Fig. 3. Comparison of the nanohardness of magnesium alloy AZ31 protected by the carbon coating deposited under optimum conditions of PACVD process and the specimen without this coating

The latter presents the difference between the nanohardness of magnesium alloy AZ31 protected by the hard carbon coating deposited under optimum conditions of PACVD process and the alloy without this coating. These results provide evidence that the nanohardness of magnesium alloy AZ31 protected by the hard carbon coating deposited by the PACVD method was considerably higher (24 GPa) than that of the alloy without the coating (0.8 GPa).

3.3 Determination of the thickness of hard carbon coating

The thickness of hard carbon coatings was determined by the method of direct profilography using the highly precise Taylor Hobson profilographometer (Golabczak, 2005, 2010). To achieve the accurate results of measurements, the carbon coatings were deposited only on selected fragments of the examined samples of magnesium alloy. Therefore, some parts of their surface were protected by quartz plates during synthesis of the coatings (Fig. 4). Thus the examined surfaces of magnesium alloy contained the fragments coated by the carbon layer and free from the latter. Results of these measurements are collected in figure 5. The mean value (from 5 distinct measurements) of the thickness of a carbon coating was approximately 220 nm.

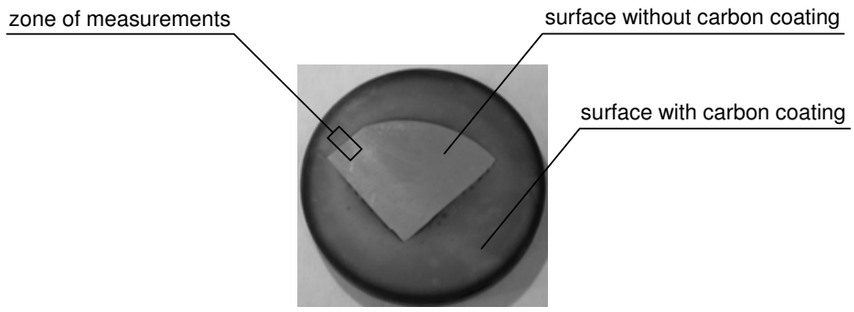

Fig. 4. The image of the surface of a specimen of magnesium alloy AZ31 prepared for the measurements of hard carbon coating thickness and the zone of measurements carried out by profilography method

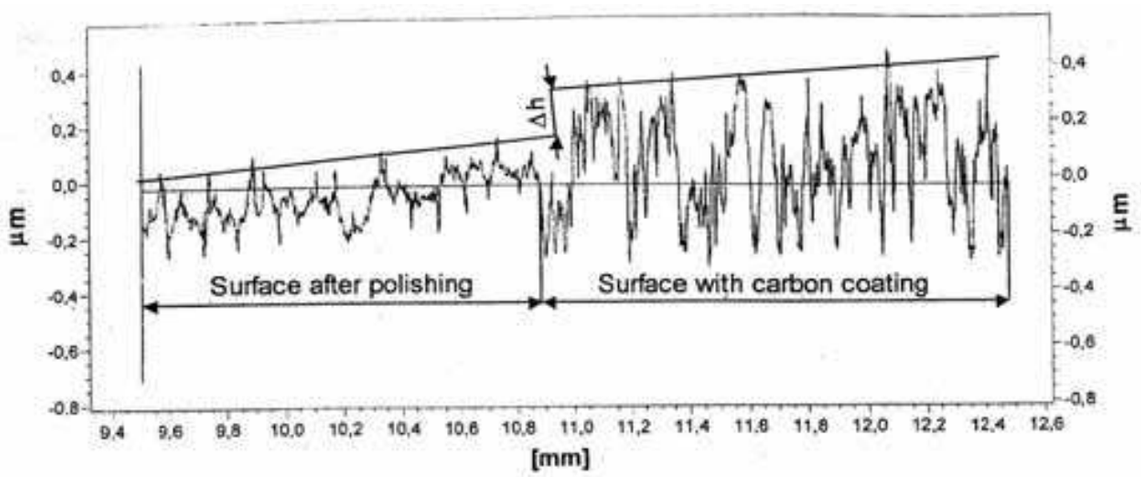

Fig. 5. Results of measurements of the thickness of hard carbon coating deposited on magnesium alloy AZ31 carried out by the method of direct profilography; the thickness of hard carbon coating (Δh) is equal to 220 nm

3.4 Tribologic measurements of hard carbon coatings

Tribologic measurements relied on tests of rubbing interaction between rectangular specimens of magnesium alloy AZ31 covered by the carbon coating and deprived of this layer with the cylindrical rubbers (Golabczak, 2005). The rubbers were prepared from three different materials such as hydrogenated rubber butadiene-acrylonitrile – HNBR, poly(methylmetacrylate) – PMMA (plexsiglass), and poly(tetrafluoroethylene) – PTFE (teflon). Dimensions of rectangular specimens of magnesium alloy were 10x4x5mm. The cylindrical rubbers had the diameter of 35mm and width of 10mm. Tribologic tests were conducted using Tribometer T-05 under the following conditions: normal load of the rubber – 6N, the rubbing speed – 3.67 cm/ s, time of test duration – 2h, frequency of recording of measurements – 2E+14, and ambient temperature (T) of 20.7°C. Representative results of tribologic measurements are shown in figure 6-7. They present differences in the total friction energy and volumetric wear of the examined specimens during the test. The displayed results provide evidence that the carbon coatings deposited on magnesium alloy considerably improve its properties. They both reduce the total energy of friction and enhance their resistance to wear. Our experiments revealed that the total energy of friction of the listed above specimens with carbon coatings, was considerably lower and reached: 44% for the rubber one, 130% for the plexiglass rubber and 440% for that made of teflon. Carbon coatings also significantly decreased the total volumetric wear of the examined samples of magnesium alloy. The relative increase in wear resistance was: 660% – in case of the rubber rubber, 540% – for the plexiglass rubber and 800% – for the teflon one.

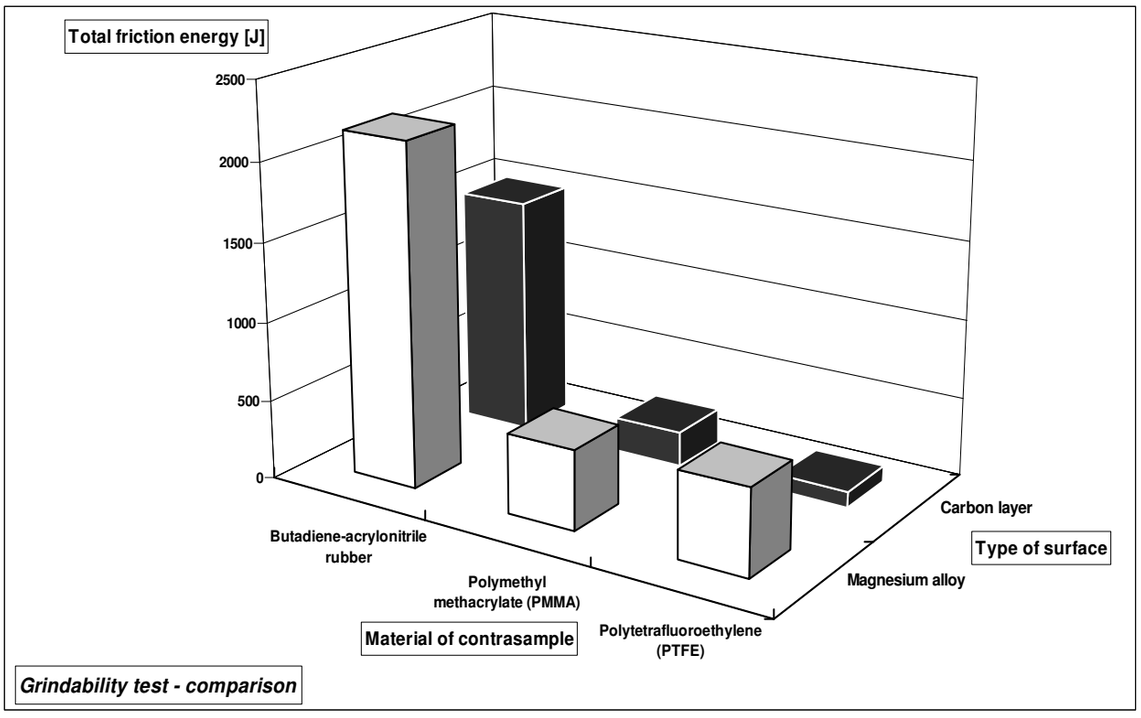

Fig. 6. Comparison of values of the total energy of friction determined by tribologic measurements for specimens of magnesium alloy AZ31 protected by the hard carbon coating and without the latter

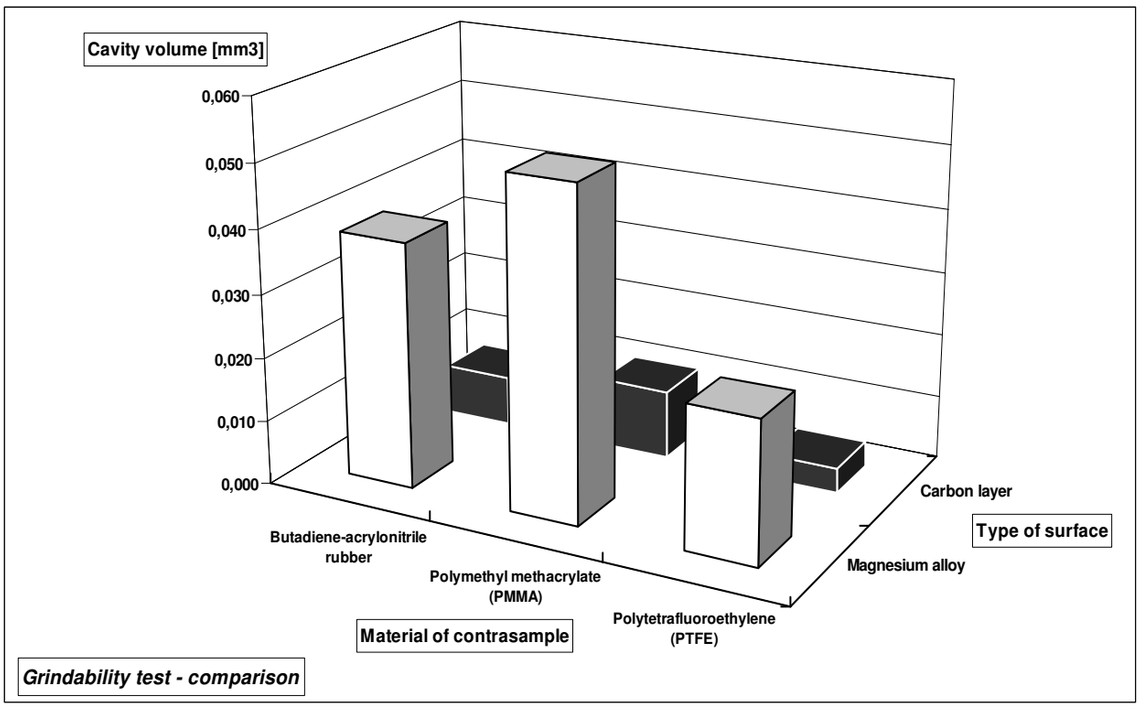

Fig. 7. Comparison of volumetric wear of the specimens of magnesium alloy AZ31 (one covered by the hard carbon coating and the second – without this coating) determined by tribologic measurements

3.5 Determination of corrosion resistance of hard carbon coatings in the salt spray chamber

Corrosion resistance tests of hard carbon coatings were conducted in SIGMA DIESEL salt chamber (BOSCH) (Golabczak, 2005). The examined specimens of magnesium alloy AZ31 were either protected with the carbon coating or not. Test conditions are displayed in table 3. The samples without the carbon coating were exposed to sodium chloride solution for 5h while the samples protected by this coating were exposed for 200h.

Test parameters	Value
Time of test duration	5h and 200 h
Temperature in the chamber	35°C ± 1°C
Humidity in the chamber	85% - 90%
Intensity of spraying (the sprayed surface area of 80 cm^2)	2ml ± 1ml / h
Air pressure	1.0 bar ± 0.2 bar
NaCl concentration in the solution	5% (w/ v)

Table 2. Parameters of corrosion test carried out in a salt spray chamber

To estimate results of the corrosion test, images of the surface of specimens, which were subjected to this test were recorded using two microscopes, i.e. metallographic and SEM. Representative images of the surface of examined specimens are shown in figure 8 and 9.

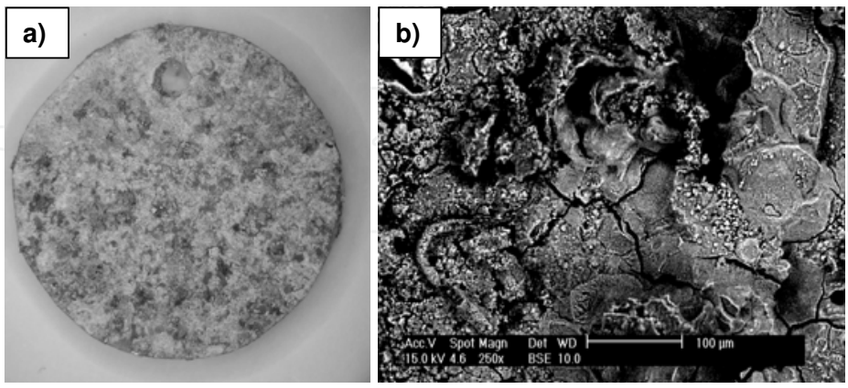

Fig. 8. Microscopic images of AZ31 magnesium alloy specimens without the hard carbon layer after 5h exposition in a salt spray chamber: a) magnification 3x, b) magnification 250x

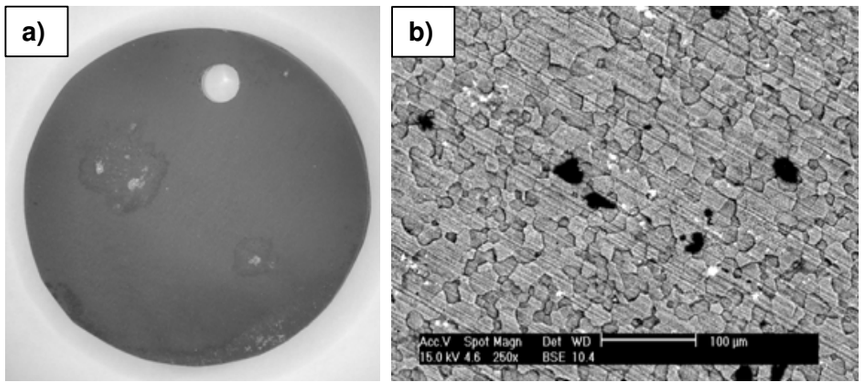

Fig. 9. Microscopic images of AZ31 magnesium alloy specimens with deposited hard carbon layer after 200h exposition in a salt spray chamber: a) magnification 3x, b) magnification 250x

Comparison of the images of surface of specimens of magnesium alloy AZ31 exposed to the corroding environment in a salt chamber showed that the samples, which were not protected by the carbon coating were strongly corroded after the relatively short time of exposition (5h). In contrast, the specimens coated by the carbon film contained only small pits of corrosion after 200h of treatment under the same conditions. Results of these experiments demonstrate that carbon coatings explicitly protect magnesium alloy from corrosion.

3.6 Determination of corrosion resistance of hard carbon coatings using electrochemical method

The accelerated electrochemical method consisted in repeated potentiostatic measurements carried out by using Volta Master 1 set comprising a potentiostat Radiometr-Copenhagen PGP 201. The examined samples were immersed in Tyrod's electrolyte (its chemical composition is shown in table 3) at the temperature of 20°C.

NaCl [g/ dm³]	$CaCl_2$ [g/ dm³]	KCl [g/ dm³]	NaH_2PO_4 [g/ dm³]	$MgCl_26H_2O$ [g/ dm³]	NaHCO [g/ dm³]	pH
8.00	0.20	0.20	0.05	0.10	1.00	6.9

Table 3. Chemical composition of Tyrod's electrolyte

Modeling of phenomena occurring at the contact interface between the conductor (metal) and the electrolyte was based on the standard Butler-Volmer equation (Golabczak, 2008). It is a half-empirical equation and characterizes the rate of electric charge transfer through the interface of phases: metal-electrolyte. This rate depends, first of all, on the difference of potentials and its sign (positive or negative) at this interface. The analysis of current flow through the medium which is far from the state of equilibrium cannot be done without the model of Butler-Volmer. The model based on an electric nonlinear circuit was proposed to determine the flow of current in the wide range of potential values. This circuit contains some elements responsible for individual physical phenomena that take place during potentiostatic measurements. The scheme of this substitute circuit is shown in figure 10.

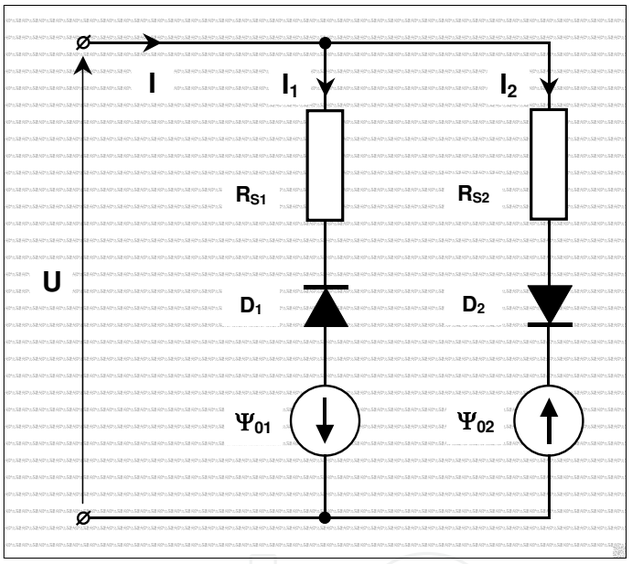

Fig. 10. The structure of proposed model in the form of the nonlinear electric circuit with lumped constants

The proposed model consists of two branches characterizing anodic and cathodic currents. Relationships between the elements of the model shown in figure 10 and phenomena occurring at the interface conductor-electrolyte are as follows:

- diodes D_1 and D_2 that are fundamental elements of the proposed model correspond to the exponential components of Butler-Volmer equation that are responsible for diffusion ,
- resistors R_{S1} and R_{S2} are responsible for the transfer of electric charge carriers and are particularly important at higher values of voltage U,
- voltage generators Ψ_{01} and Ψ_{02} are responsible for the difference in potentials at the contact interface for anodic and cathodic parts of the characteristics.

Equations describing the substitute electric circuit (Fig. 10) are as follows:

- for the anodic branch (left parts of descending curves in figure 11 and 12):

$$j_1 = -j_{01}\left(e^{-\frac{q\cdot m_1}{k\cdot T}\cdot U_{D1}} - 1\right) \tag{3}$$

- for the cathodic branch (right parts in ascending curves in figure 11 and 12):

$$j_2 = j_{02}\left(e^{\frac{q\cdot m_2}{k\cdot T}\cdot U_{D2}} - 1\right) \tag{5}$$

The total current flowing through the interface is the sum of anodic current and cathodic current:

$$j = j_1 + j_2 \tag{7}$$

where: q- the elementary charge of an electron, expressed in [C] [A·s], q=1.6022·10^{-19} C;
k- Boltzman constant, expressed in [J/ K] [kg·s^2/ m^2·K], k=1.3807·10^{-23} J/ K;
T- the temperature of the contact interface [K];
j_{01}, j_{02} – the density of saturation currents, expressed in [mA/ cm^2];
R_{S1}, R_{S2} – resistances representing the phenomenon of electron transfer, expressed in [Ω];
m_1, m_2 – coefficients dependent on division of currents and valences of ions in the electrolyte, dimensionless quantities.

Electric parameters of this model for individual potentiostatic curves (Tafel curves) were identified by means of the least square method and by resolving the system of nonlinear equations by the gradient method. The obtained parameters are effective estimators of the true model parameters. Results of potentiostatic measurements were plotted in figure 11 and 12. Intercepts of curves presenting the voltage on diodes with OX axis correspond to potentials on the interface metal-solution. The values of electric parameters that were calculated for the assumed models are presented in table 4 and 5. On completion of potentiostatic measurements the surface of the examined samples was subjected to SEM analysis. Examples of the recorded images are shown in figure 13 and 14. Analysis of results of electrochemical studies revealed that deposition of the hard carbon coating on the surface of AZ31 magnesium alloy significantly dislocated and increased the difference in potentials (corrosion potential increased) at the interface between the metal and solution (Fig. 12) as compared to the reference sample without the coating (Fig. 11). It provides evidence of the beneficial effect of hard carbon coating deposited on this alloy because the barrier protecting the latter from electrochemical corrosion was increased.

Model parameters	J_0	Ψ_0	m	R_S
	mA/cm^2	V	-	Ω
Diode I	0.009145	-1.6622	0.4276	1092.46
Diode II	0.000100	-1.6482	0.9607	643.96
Fitting error		4.027E-03		
Deviation 3σ		5.280E-02		mA/cm^2

Table 4. Electric parameters of the potentiostatic curve of electrochemical corrosion for sample made of AZ31 magnesium alloy free of carbon coating

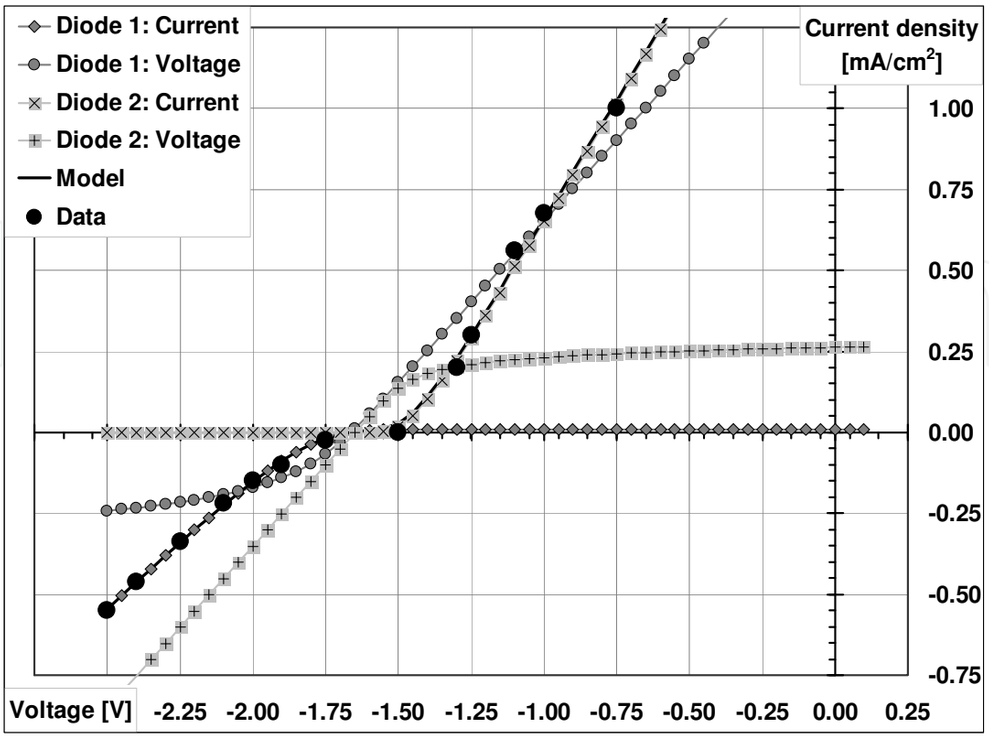

Fig. 11. Potentiostatic curve of electrochemical corrosion for AZ31 magnesium alloy free of hard carbon coating

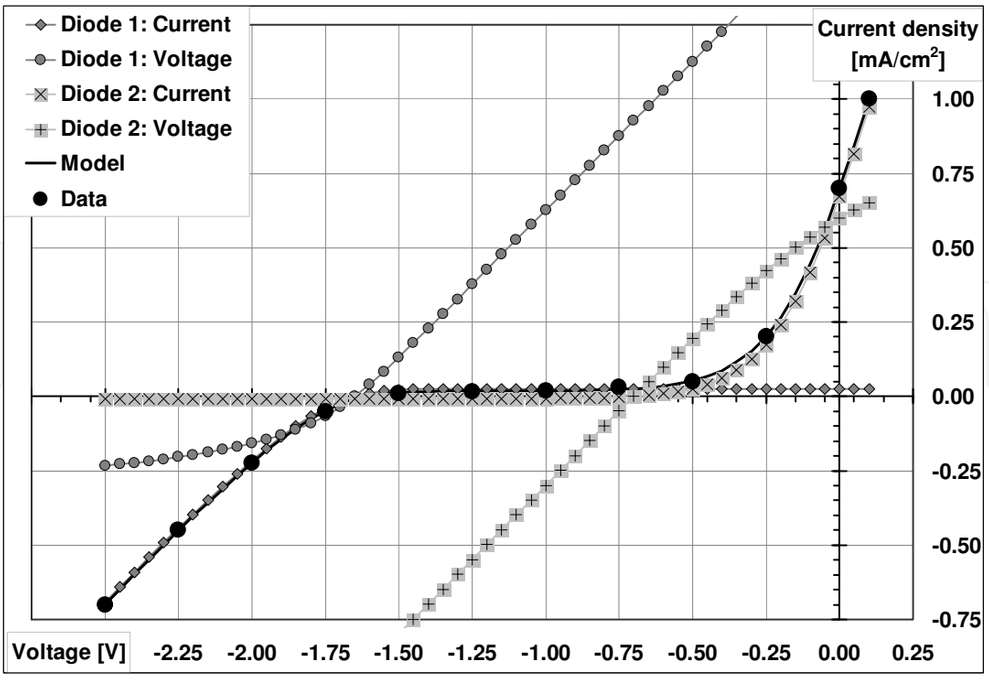

Fig. 12. Potentiostatic curve of electrochemical corrosion for AZ31 magnesium alloy protected by hard carbon coating

Model parameters	J_0	Ψ_0	m	R_S
	mA/cm^2	V	-	Ω
Diode I	0.026058	-1.6501	0.3588	892.26
Diode II	0.008067	-0.7000	0.1867	152.36
Fitting error		7.947E-05		
Deviation 3σ		7.720E-03		mA/cm^2

Table 5. Electric parameters of the potentiostatic curve of electrochemical corrosion for sample made of AZ31 magnesium alloy bearing the carbon coating

Also SEM analysis of the surface of the examined samples confirmed this desirable impact (Fig. 13 - 14). Only single dark spots (probably very small corrosion pits) were visible at the surface of the samples bearing hard carbon coating (Fig. 13) whereas harmful results of electrochemical corrosion were visible on the whole surface of unprotected AZ31 magnesium alloy (Fig. 14).

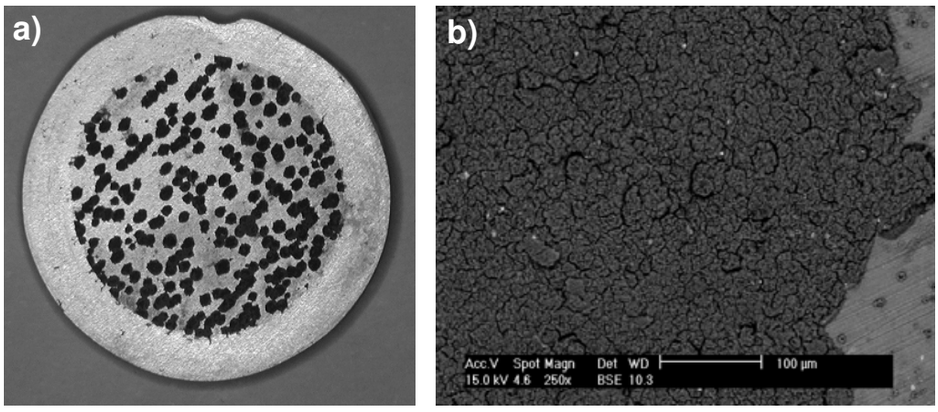

Fig. 13. SEM image of AZ31 magnesium alloy surface on completion of the potentiostatic corrosion test; test duration-1h: a) magnification 3x, b) magnification 250x

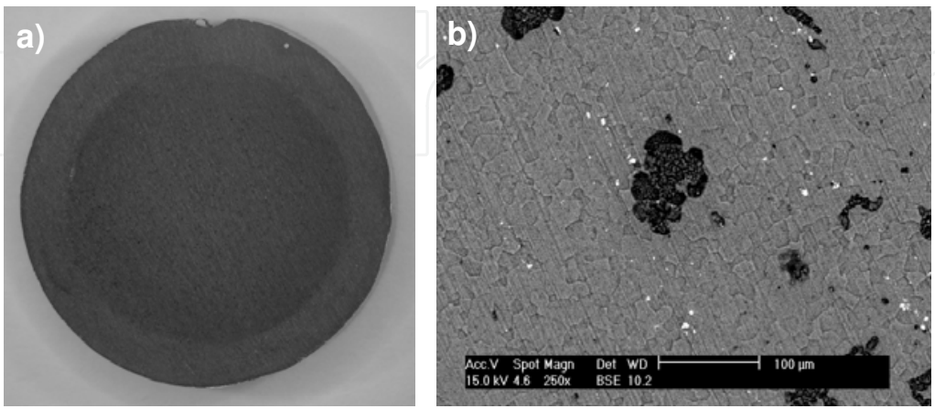

Fig. 14. SEM image of the surface of AZ31 magnesium alloy protected by hard carbon coating on completion of the potentiostatic corrosion test; test duration 1h: a) magnification 3x, b) magnification 250x

4. Raman spectra evaluation of the hard carbon layers

Raman effect has been widely used for carbon layers analysis from years for qualitative analysis of samples as well as quantitative. Two main lines of attitude to the quantitative analysis of the Raman spectra have been developed. The first one is applied mainly in forensic investigations when one have prepared comparative sample consist of known substances with known concentration which is the base for comparison of spectra from unknown sample. A tool used in these investigations is Voigt profile based on Faddeeva function, allowing a very precise comparison of spectra with elimination of individuality of measurement equipment. This attitude seems not to be the best solution when one has not comparative samples and sample under test is unique – the situations often meet in scientific investigation. Using Voigt profiles may cause a lost of information carried with spectrum, especially related with small quantities of nanotubes or fullerenes generated in the process of imposing diamond layers in plasma arc. Another function for approximation shape of the Raman peak based on Breit-Figner-Fano curve is frequently used but difficulties arise when identifying physical meaning of parameters and subtracting idle pedestal from the experimental spectrum. A different attitude based on simple Gaussian peak approximation has been discussed leading to the conclusion, that engaging more advanced and sophisticated methods does not provide automatically better results. Especially for coatings used in health care very careful evaluation of the experimental data have to be performed (Golabczak & Konstantynowicz, 2009). In this paper we would like to deal more deeply with Voigt profile matching to the Raman spectrum taking into account the measurement equipment characteristics, i.e. filtering efficiency of the Fabry-Pérot interferometer. Accordingly the figure 15 mutual relationship between wave of the wave number k_S being anti-stokes scattered and detected with Fabry-Pérot interferometer and incident laser wave of the wave number k_L is given by the so called Raman shift denoted k_R:

$$k_S - k_L = k_R \tag{8}$$

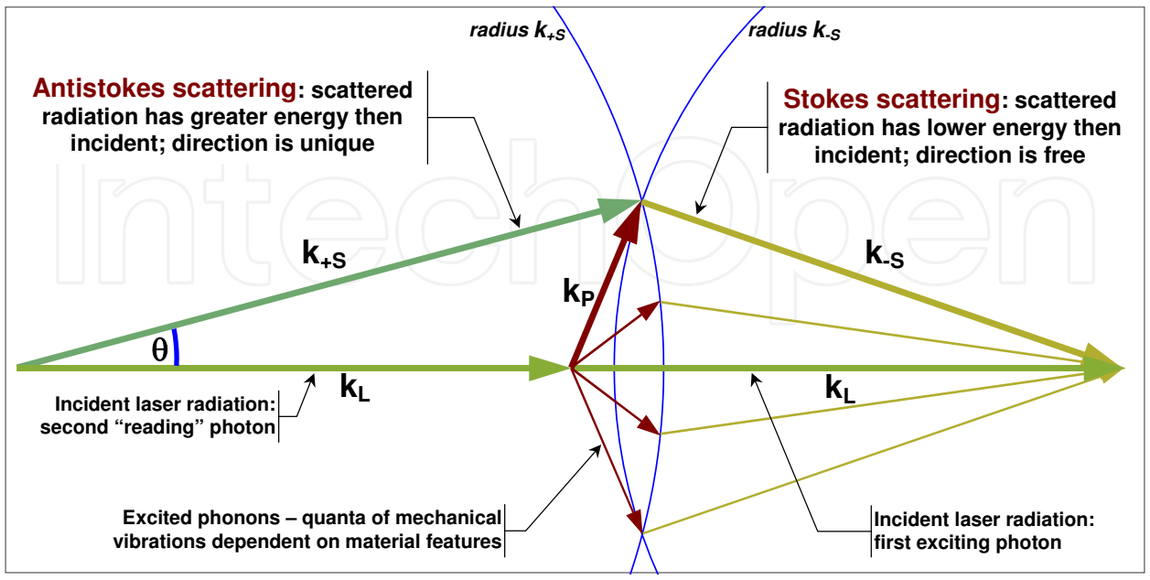

Fig. 15. A schematic diagram of the Raman scattering mechanism (multi-photon/ fonon interaction)

Passing to the wavelength domain gives:

$$\frac{2\pi}{\lambda_S} - \frac{2\pi}{\lambda_L} = k_R \tag{9}$$

Finally we obtain relationship used further:

$$\lambda_S = \frac{\lambda_L}{1 + \lambda_L \cdot \frac{k_R}{2\pi}} \tag{10}$$

Obviously, all of the length units in the equation (10) have to be the same. It is worth of memory, that wavelength of the laser emitted beam is usually given in [nm] (10^{-9} m) and Raman shift wave number is given in [cm^{-1}] (10^{-2} m) as a rule. The relationship (10) allows us to draw the Raman spectrum from an experiment in the wavelength domain, which is dependent on the laser beam wavelength. Following, it allows comparison of the Raman spectrum with the Fabry-Pérot interferometer characteristics evaluated traditionally in the wavelength domain (Golabczak & Konstantynowicz, 2009). Accordingly this rule Raman spectrum has been drawn in the figure 19 showing the simulated Fabry-Pérot interferometer characteristics interaction with the Raman spectrum from an experiment. In this paper we have been used Raman spectrum investigation for determining both layer composition and quantitative determination of the diamond-like structure participation in the layer. Examination of the layer imposing procedure shows, that different carbon allotropes or compounds could be expected in the layer, not only diamond-like (Golabczak & Konstantynowicz, 2009). Although efforts have been made to enhance content of the diamond-like structures is not possible to obtain a pure one. In our further works related with optimization of the layer content, especially assuring proper balance between diamond and graphite structures, we will need especially precise tools for quantitative examination of the layer, presumably more precise then tools based on the standard Raman spectrum profile matching for recognition purpose only.

4.1 The Voigt profile basics

In the paper we have examined use of different functions modeling shapes of the Raman spectrogram for different purposes. Here we like to deal in details with Voigt profile use and computational problems. Voigt profile is a specific convolution function, with two parameters, which covers features of the Raman spectrum generated by the investigated material features as well as the influence of the Fabry-Pérot interferometer used as the detector:

$$V(x,\sigma,\gamma) = \int_{-\infty}^{+\infty} G(t,\sigma) C(x-t,\gamma) dt \tag{11}$$

where: $G(x,\sigma)$ - central Gaussian (with zero mean value) distribution modeling features of the investigated material, given as the probability distribution function with one parameter σ determining its width:

$$G(x,\sigma) = \frac{1}{\sigma\sqrt{2\pi}} e^{-\frac{x^2}{2\sigma^2}} \tag{12}$$

$C(x,\gamma)$ - central Cauchy distribution modeling influence of the Fabry-Pérot interferometer, called also "Lorentz distribution", given as the probability distribution function with one parameter γ determining its width:

$$C(x,\gamma)=\frac{\gamma}{\pi\left(x^2+\gamma^2\right)} \tag{13}$$

In closed form, after performing integration in convolution, Voigt profile can be expressed as:

$$V(x,\sigma,\gamma)=\frac{\mathrm{Re}[F(z)]}{\sigma\sqrt{2\pi}} \tag{14}$$

where complex z variable is of the form:

$$z=\frac{x+j\gamma}{\sigma\sqrt{2}} \tag{15}$$

where in turn $F(z)$ is complex complementary error function called also Faddeeva function.

$$F(z)=e^{-z^2}erfc(-jz) \tag{16}$$

where in turn:

$$erfc(z)=1-erf(z) \tag{17}$$

is the complementary error function of the complex variable expressed as (non-analytical!) integral:

$$erfc(x)=\frac{2}{\sqrt{\pi}}\int_x^{\infty}e^{-t^2}dt \tag{18}$$

Effective computation of the *erfc* function i.e. fast and precise even for relatively big $|z|$, and the following computation Faddeeva function, establish a real problem. A number of methods is known, sometimes assuming very specific use in spectrum recognition, eq. (Estevez-Rams et al., 2005). They are all based on different approximations of the $F(z)$ function (power series expansions) easy (relatively!) for computation (Di Rocco et al., 2004; Ida et al., 2000). Sometimes these approximations are very specific and not usable beside rare programming environments or operating systems.

A universal and effective computation of the complex error function at the given point can be also performed traditionally by expansion in the Taylor power series (Abramowitz et al., 1968), which seems to be more practical then basing upon the very special functions one can meet only in a few types of processors or programming languages:

$$erf(z)=\frac{2}{\sqrt{\pi}}\sum_{n=0}^{\infty}\frac{(-1)^n z^{2n+1}}{n!(2n+1)} \tag{19}$$

from (13), (14) and (16) we obtain:

$$F(z) = e^{-z^2}\left(1 - \frac{2}{\sqrt{\pi}}\sum_{n=0}^{\infty}\frac{(-1)^n z^{2n+1}}{n!(2n+1)}\right) \tag{20}$$

Computing of the series (17) can be speed up with using two goals:

- iteratively counting each next summand from previous – it is so called conversion into multiplicative form of the (16) expression;
- performing full complex multiplication in algebraic form, not passing to trigonometrical functions which computation is the most long-lasting elementary operation.

Preserving of the about 30 terms in power series allows to compute complex error function with relative error less than 10^{-10} in the neighborhood of center which is enough for most of the purposes. Increasing the number of terms to about 250 allows to compute function with the precision of 10^{-15} even at the radius of $|z|$ at the level of 5. This has been computationally proven in our practice.

Plots of the described functions are depicted on the figure 16 and 17., where comparison has been made among peaks for different γ parameter related with Fabry-Pérot interferometer used in an experiment.

4.2 The Fabry-Pérot interferometer

The Fabry-Pérot interferometer was developed in 1899 as a device for the very precise measurement of the length with using visible light wave as a "ruler". This is also the origin of its other name – an "etalon". Because of its excellent abilities in electromagnetic waves filtering in very narrow bands it has soon became a valuable tool in spectrometry. It is comprised of the two parallel surfaces reflecting light or electromagnetic wave from the other range eq. infrared or ultraviolet. Light is reflected and transmitted through the interferometer plate and reflected internally many times. Incident beam interfere with internally reflected, which gives an effect of selective passing the electromagnetic wave through the plate in the very narrow bands – transmission windows. This process is depicted schematically on the figure 18 where one of the possible configurations is considered. More sophisticated constructions based on two wedged plates are in use as well as the three plates assemblies, however this simply scheme covers the scope of our investigations with sufficient precision (Flowles, 1989). Preserving of the paralellnes of the surfaces is essential for the precision of the interferometer both in making the transmission window as narrow as possible and assuring that it is set in the prescribed point of the whole spectrum (Hernandez, 1986). This precision is in the scope of our special attention and will be practically identified from Raman spectrograms. We have been considered also with the tuning mechanisms of the Fabry-Pérot interferometers, but at this stage of investigations we have found them neglectable.

Spatial phase difference between two consecutive beams internally reflected – see figure 18 is given by the equation, setting up base relationship in the Fabry-Pérot interferometer analysis:

$$\delta = \frac{2\pi}{\lambda}\cdot 2\cdot n(\lambda)\cdot d\cdot\cos(\theta) \tag{21}$$

where: λ - wavelength of the incident electromagnetic radiation, [m];

$n(\lambda)$ – refraction index of the material between reflecting surfaces, variable along the wavelength of the radiation, [-];

d – distance between reflecting surfaces, normally is the thickness of the plate, eq. made of quartz crystal or quartz glass, which surfaces are silvered, [m];

θ – angle between normal to the plate surface and incident beam of radiation, [rad].

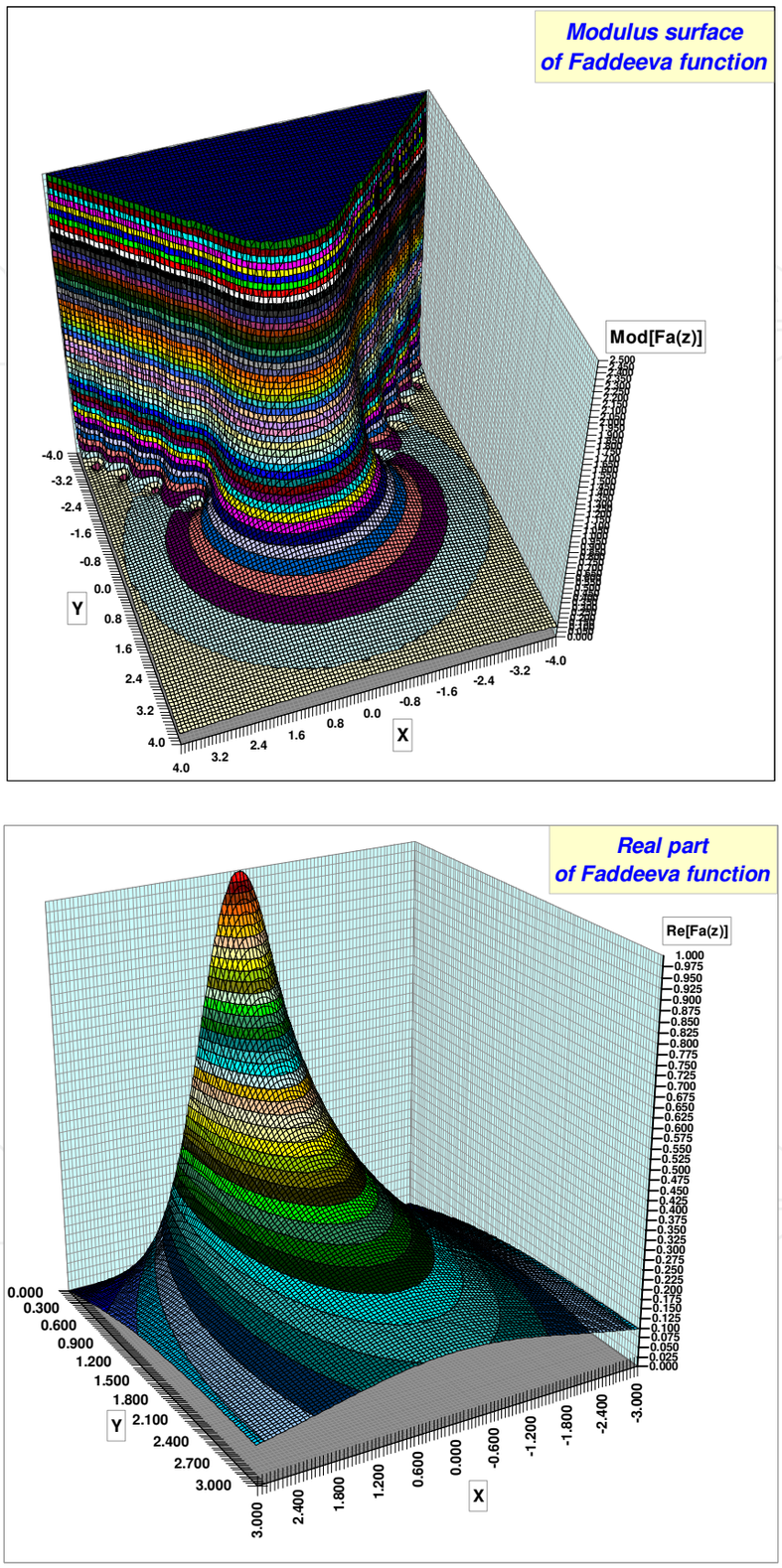

Fig. 16. Complex error function (Faddeeva function): modulus surface and real part surface

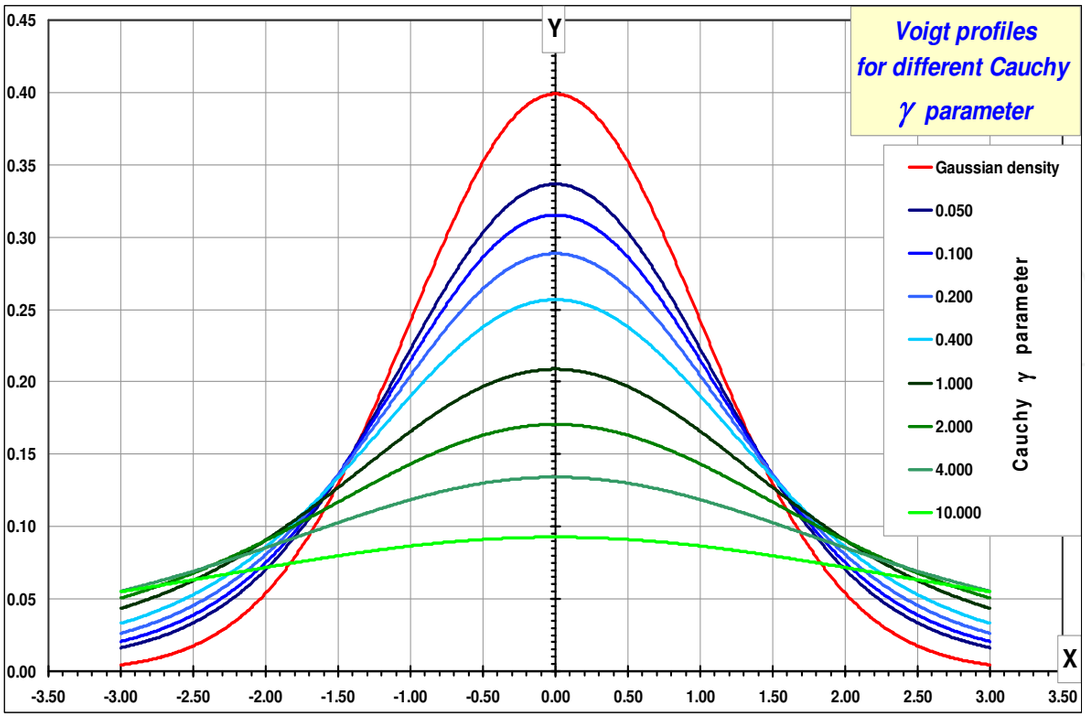

Fig. 17. Comparison of the Voigt profiles made of the normalized Gaussian density and the Cauchy densities of different width parameters γ

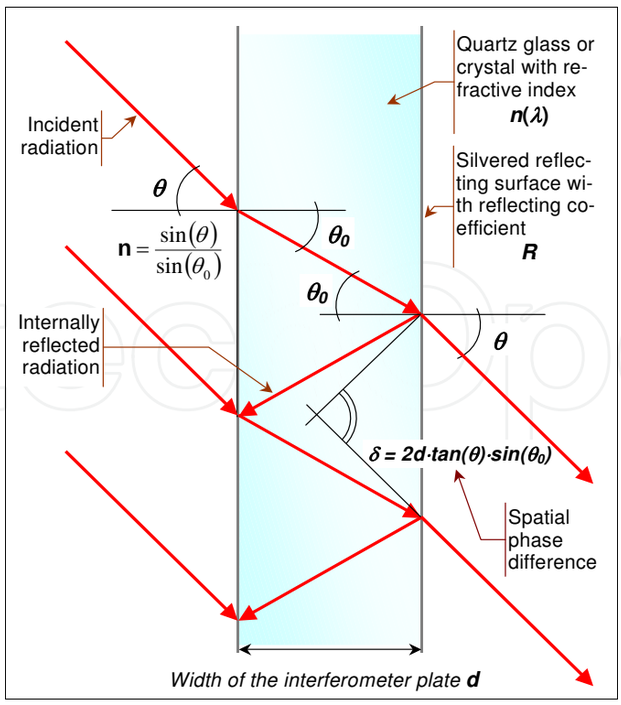

Fig. 18. Schematic diagram of the simply Fabry-Pérot interferometer and subsequent reflections of the interfering light beams.

Infinite summation of the series of reflections gives well-known Airy formula for transmission coefficient T_E of the interferometer as the function of its construction parameters, wavelength of the radiation and direction of the radiation toward interferometer plate:

$$T_E = \frac{(1-R)^2}{1+R^2-R\cdot\cos(\delta)} = \frac{1}{1+F\cdot\sin^2\left(\frac{\delta}{2}\right)} \tag{22}$$

where: R – coefficient of the reflection assumed the same for both surfaces, [-];
F – finesse coefficient of the Fabry-Pérot interferometer:

$$F = \frac{4R}{(1-R)^2} \tag{23}$$

Coefficient of the maximal reflection of the interferometer plate – between spectral windows is given by:

$$R_{\max} = \frac{4\cdot R}{(1-R)^2} \tag{24}$$

Distance between consecutive spectral windows i.e. peaks of the interferometer characteristics – see figure 19, so called FSR – *Free Spectral Range* of the interferometer, which describes the range of unambiguous measurements, is given by the equation:

$$FSR = \Delta\lambda = \frac{\lambda_0^2}{\lambda_0 + 2\cdot n(\lambda_0)\cdot d\cdot\cos(\theta)} \tag{25}$$

where: λ_0 – wavelength of the peak to whom the FSR is associated when the plate is set appropriately to pass this peak through, [m];

- the rest of variables as in the previous equations.

Shape determination of the peak (transmission window) of the Fabry-Pérot interferometer have to be done at the fixed θ, i.e. for the fixed value of wavelength λ_0 in the center of the peak with corresponding wave number $k_0 = 2\pi/\lambda_0$ and for the current variable $k = k_S - k_0$ as:

$$\frac{\delta}{2} = (k_S - k_0)\cdot n\cdot d\cdot\cos(\theta) = (k_S - k_0)\cdot c_F \tag{26}$$

where: c_F – coefficient, constant in the contiguity of the peak, [m]:

$$c_F = n(\lambda_0)\cdot d\cdot\cos(\theta_0) \tag{27}$$

The relationship between T_E and wave number of the incident radiation should be determined in the nearest vicinity of the peak's center, for the very small values of the δ angle when one can use the approximation $sin(x) \approx x$:

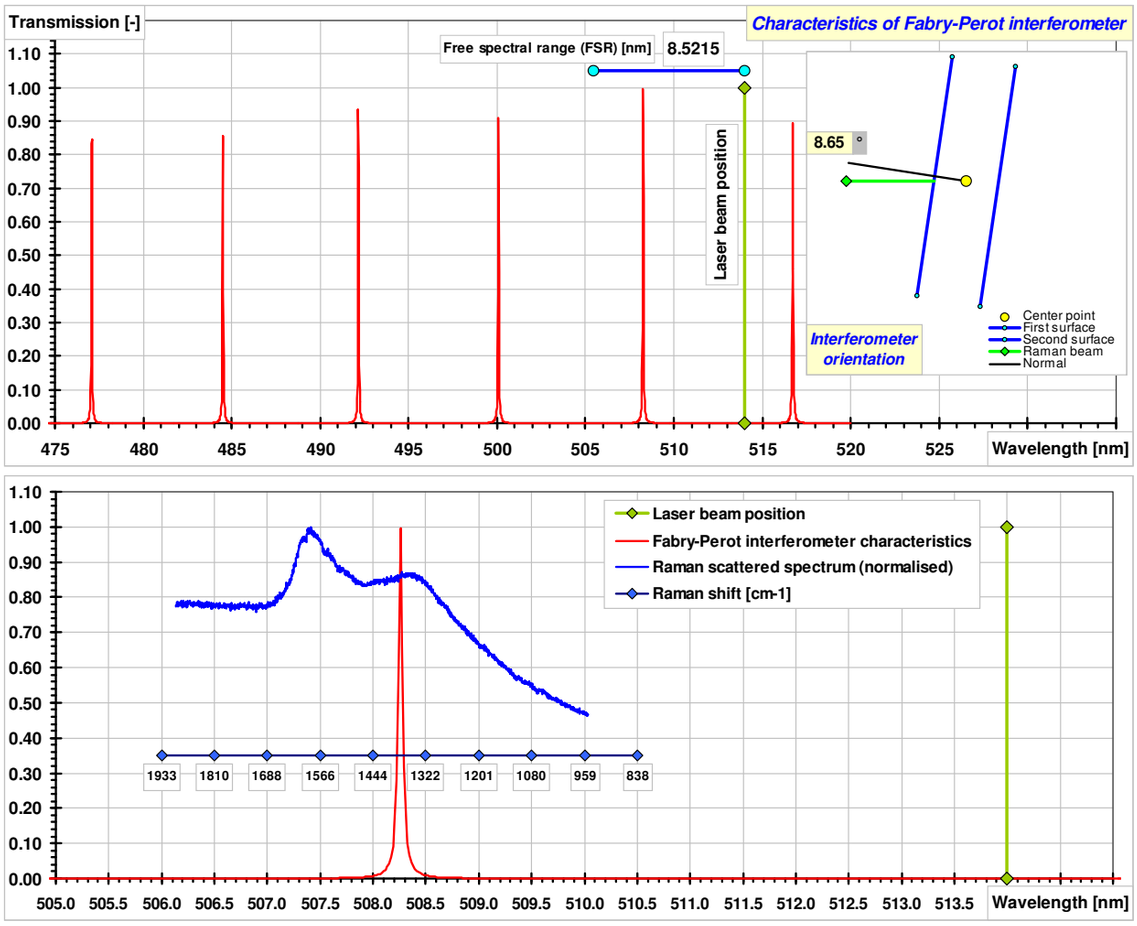

Fig. 19. Simulated characteristics of the Fabry-Pérot interferometer used in the Raman spectrum analyzer. Parameter γ of the interferometer has been extracted from the Voigt profile matched to the Raman spectrum from an experiment, which has been exposed in the background of the lower diagram. The lower diagram is to scale!

$$T_E = \frac{1}{1 + F \cdot \sin^2\left(\left(k_S - k_0\right) \cdot c_F\right)} \cong \frac{\dfrac{1}{F \cdot c_F^2}}{\dfrac{1}{F \cdot c_F^2} + \left(k_S - k_0\right)^2} \tag{28}$$

It follows from the equation (25) that the spectral peak placed at the wave number k_0 has the shape described by the curve of the type (10), i.e. Cauchy/ Lorentz, where:

$$\gamma = \frac{1}{c_F \cdot \sqrt{F}} \tag{29}$$

The equation (26) allows relating constant γ derived during matching the Voigt profile based function to the Raman spectrum, with technical parameters of the Fabry-Pérot interferometer used as the detector of the scattered radiation. Let make this evaluation for

the interferometer which characteristics is depicted on figure 19. We have assumed the following construction parameters (realistic!):

- Wavelength of the laser radiation: $\lambda_L = 514$ nm (green-yellowish light);
- Material of the interferometer plate: quartz glass;
- Refraction coefficient of the plate material at laser wavelength: $n = 1.461582$;
- Plate thickness (after tuning of course): $d = 10.5503$ μm = 10550.3 nm;
- Reflection coefficient of the silvered surface: $R = 0.982900$;
- Finesse of the interferometer: $F = 13445.5$;
- Order of the used peak: $m = 30$;
- Free spectral range: $FSR = 8.5295$ nm;
- Parameter γ describing peak shape from equation (19): $\gamma = 5.66$ cm^{-1};
- Extraction of the γ parameter of the Fabry-Pérot interferometer from the Voigt profile matched to the real Raman spectrum from an experiment – investigation of the hard carbon layer imposed with PACVD method on the magnesium alloy, has gave mean value for the all peaks and spectra: $\gamma \approx 5.66$ cm^{-1}

It could be easily seen that matching of the Voigt profile based function has provided us with the very realistic evaluation of the γ parameter. What more this parameter has happen to be at the same level for all the peaks and all the matched spectra. A sample matching result is depicted on the figure 20 showing plenty of different carbon forms, which one can expect in the layer. The spread of the γ parameter for all the five matching spectra is exhibited on the figure 21.

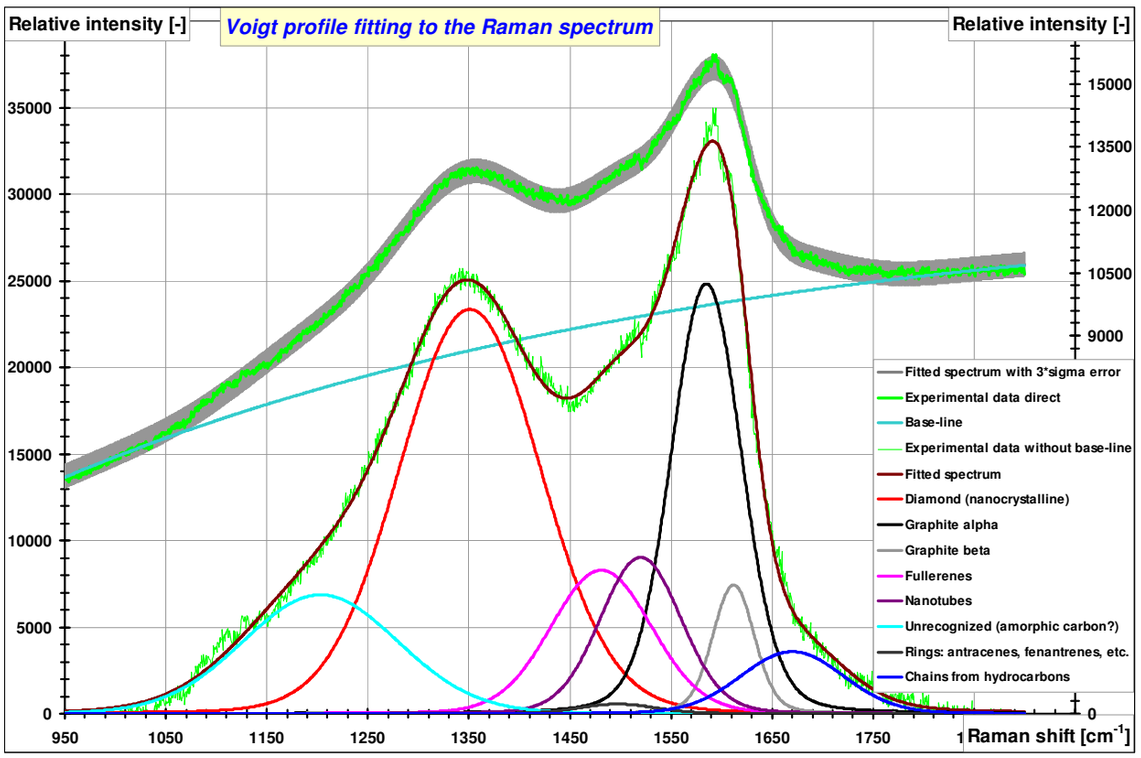

Fig. 20. Matching of the Voigt profile based function to the Raman spectrum of the DLC layer imposed on the light alloy

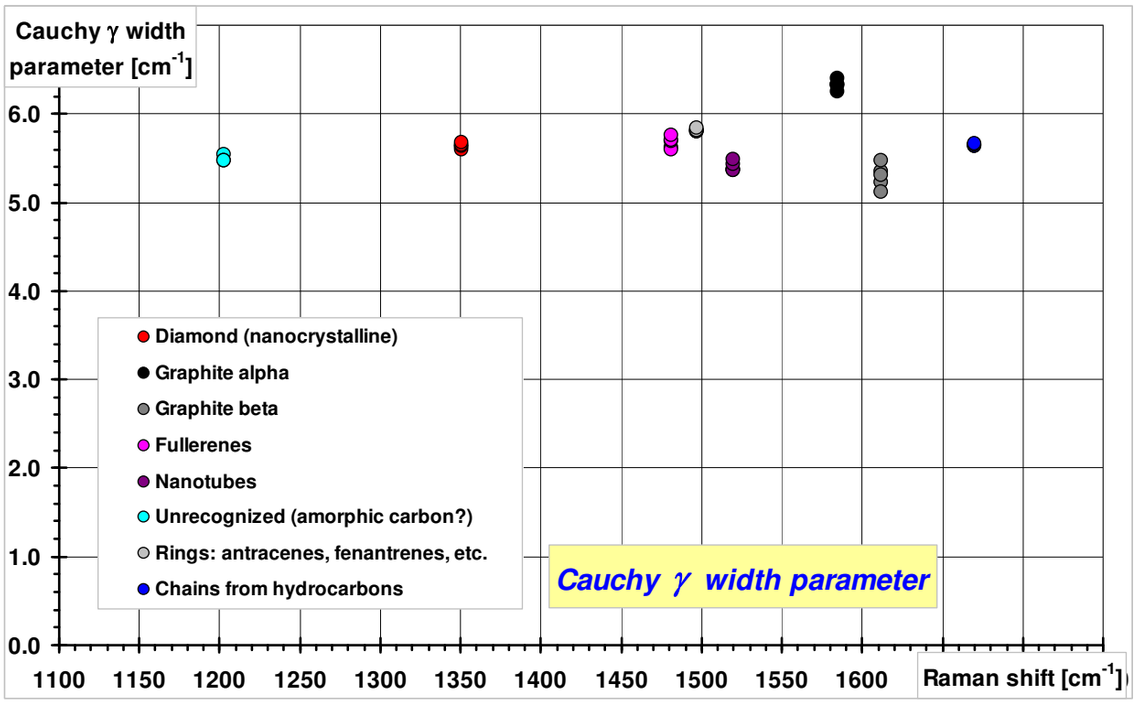

Fig. 21. Distribution of the γ parameter for all the analyzed peaks in the five Raman spectra of the hard carbon layers

4.3 The Voigt profile matching to the Raman spectra

The profile formulas, which could be matched to the Raman spectra, were discussed in details from metrological point of view in this paper (Golabczak & Konstantynowicz, 2009). Here we have used Voigt profile based function:

$$I_V(k) = \sum_{n=1}^{N} I_{0_n} \cdot V\left(k - k_{0_n}, \sigma_n, \gamma_n\right) + \\ + \left(I_{B_{MAX}} - I_{B_{MIN}}\right) \cdot \left(1 - \exp\left(-S_B \cdot k\right)\right) + I_{B_{MIN}} \tag{30}$$

where: k_{0n} - wave number of the n-th peak, [m-1];
I_{0n} - maximal value of the n-th peak, [-];
σ_n - width of the Gaussian component in the Voigt profile, [m-1];
γ_n - width of the Cauchy component in the Voigt profile, [m-1].
The proper construction of the base function is a very complicated problem if one would like to relay it upon detailed deliberation about the whole spectrum of the radiation scattered when the laser beam impact sample under test. Here we have made use of a rather simple model, functional not structural, giving baseline of the spectrum (pedestal of the spectrum) as a very "flat" exponential function with three free parameters:

$$I_B(k) = \left(I_{B_{MAX}} - I_{B_{MIN}}\right) \cdot \left(1 - \exp\left(-S_B \cdot k\right)\right) + I_{B_{MIN}} \tag{31}$$

A sight at figure 18 with mutual placing of the Raman spectrum and the laser beam allows one to get additional, "visual" justification of the choose expressed in equation (31). Admitting three parameters for baseline function gives sufficient number of degrees of freedom during matching Voigt profile based function (30) to the Raman spectrum. In our case the coefficient SB was at the level about 0.0009 for all of the analyzed spectra.
All of the computations related with matching function (30) to the experimental data we have conducted in the calculation diagram built in the *Excel* spreadsheet with application the *Solver* tool. Solver seeks for the maximum or minimum of the user-prescribed function in the space of the user-prescribed variables. We have applied the following set-up to the *Solver* tool: searching for a minimum with using Newton method; scaling at each stage (iteration), square approximation of the function in the minimum vicinity, limit for searching only positive values. The number of variables was in our case as follows:

- 8 peaks with 4 parameters = 32 variables,
- baseline function: 3 parameters = 3 variables,
- total: 35 variables.

Results exhibited on figure 21 are highly reproducible from peak to peak in the given spectrum and among the Raman spectra obtained from the same spectrometer. It gives an assumption that they truly reflect quality of Fabry-Pérot interferometer and its tuning mode.

5. Conclusions

Presented studies provide evidence that PACVD method facilitates deposition of hard carbon coatings on magnesium alloy and the content of diamond phase in these coatings is high. Hard carbon coatings deposited by this method display very attractive material properties such as high nanohardness, resistance to wear, resistance to corrosion and reduced friction coefficient. Continuation of these studies aimed at the development of the devised technology of hard carbon films deposition on magnesium alloys is undoubtedly purposeful. Further research will focus on covering of items with more complicated shapes and on protecting of the inside surfaces.
Accuracy of matching the given Raman spectrum model as Voigt profile with experimental data could be improved basing on some additional information related with Raman spectrometer construction: Fabry-Pérot interferometer quality and its tuning through wavelengths expected in the Raman shift of investigated hard carbon layers manufactured on magnesium alloy. When performing Raman spectroscopy permanently with the same instrument one can include data related with this instrument, gathered from the previous spectra, in matching process of the current spectrum with Voigt profile.
Data about Fabry-Pérot interferometer gathered in our five spectrograms proved to be very homogenous. What more, some light tendency of peak broadening for higher Raman shift expressed in γ parameter decrease, correspond well with natural tendency of the Fabry-Pérot interferometer of spectral window broadening due to interferometer tuning.
Investigations described in this paper allow making some assumptions for further research: deconvolution of Raman spectra with Cauchy-type Fabry-Pérot interferometer characteristics. This should give peaks narrowing effect and then, substantial improvement in Raman spectrum recognition due to the material components detection and improvement in quantitative determination of its content.

6. References

Abramowitz, M. & Stegun, I.A. (1968). *Handbook of Mathematical Functions,* Dover Publications, New York.

Di Rocco H.O. & Aguirre Téllez M. (2004). *Acta Physica Polonica*, Vol. 106, No 6, pp. 36-48.

Estevez-Rams, E.; Penton, A.; Martinez-Garcia, J. & Fuess, H. (2005). *Crystal Research and Technology*, Vol. 40, pp. 166-176.

Flowes, G.R. (1989). *Introduction to Modern Optics,* Dover Publications, New York.

Golabczak M. (2005). *Manufacturing of Carbon Coatings on Magnesium Alloys by PACVD Method*, Technical University of Lodz, Poland.

Golabczak, M. (2008). *Mechanics and Mechanical Engineering*, Vol. 12, No 2, pp. 157-164.

Golabczak, M. & Konstantynowicz, A. (2009). *Journal of Achievements in Materials and Manufacturing Engineering*, Vol. 37, pp. 270-276.

Golabczak, M. & Konstantynowicz, A. (2010). *Defect and Diffusion Forum*, Vols. 297-301, pp. 641-649.

Gray, J.E. & Luan, B. (2002). *Journal of Alloys and Compounds*, No 336, pp. 88-113.

Hawkins, J.H. (1993). *Global View Magnesium: Yesterday, Today, Tomorrow*, International Magnesium Association, pp. 46-54.

Hernandez, G. (1986). *Fabry–Pérot Interferometers*, Cambridge University Press, Cambridge.

Ida T.; Ando M. & Toraya H. (2000). *Journal of Applied Crystallography*, Vol. 33, pp. 1311-1316.

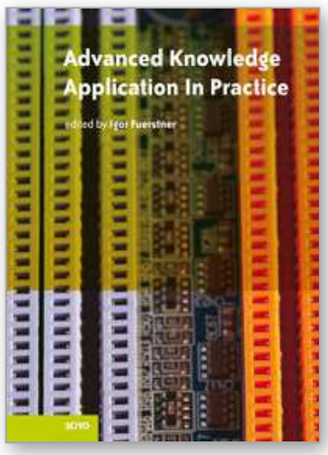

Advanced Knowledge Application in Practice

Edited by Igor Fuerstner

ISBN 978-953-307-141-1
Hard cover, 378 pages
Publisher Sciyo
Published online 02, November, 2010
Published in print edition November, 2010

The integration and interdependency of the world economy leads towards the creation of a global market that offers more opportunities, but is also more complex and competitive than ever before. Therefore widespread research activity is necessary if one is to remain successful on the market. This book is the result of research and development activities from a number of researchers worldwide, covering concrete fields of research.

INTECH
open science | open minds

InTech Europe
University Campus STeP Ri
Slavka Krautzeka 83/A
51000 Rijeka, Croatia
Phone: +385 (51) 770 447
Fax: +385 (51) 686 166
www.intechopen.com

InTech China
Unit 405, Office Block, Hotel Equatorial Shanghai
No.65, Yan An Road (West), Shanghai, 200040, China
中国上海市延安西路65号上海国际贵都大饭店办公楼405单元
Phone: +86-21-62489820
Fax: +86-21-62489821

IntechOpen